

# A comprehensive view of PKS 2155-304 from 2008 to 2023 through a multi-epoch modeling of its spectral energy distributions

G. Harutyunyan<sup>1</sup>, N. Sahakyan<sup>1</sup>, <sup>\*</sup>D. Bégué<sup>2</sup>, M. Khachatryan<sup>1</sup>

<sup>1</sup>ICRANet-Armenia, Marshall Baghramian Avenue 24a, Yerevan 0019, Armenia

<sup>2</sup>Bar Ilan University, Ramat Gan, Israel

Accepted XXX. Received YYY; in original form ZZZ

## ABSTRACT

We present a detailed investigation of the temporal and spectral evolution of the emission from the blazar PKS 2155-304, a high-synchrotron-peaked blazar. Using  $\gamma$ -ray, X-ray, optical/UV, and infrared data assembled from the Markarian Multiwavelength Data Center, we constructed multi-band light curves and temporally resolved spectral energy distributions (SEDs) of PKS 2155-304 to probe the origin of its emission. The light curves show significant variability, with fractional variability peaking at  $\sim 0.7$ – $0.8$  in soft-to-medium X-rays,  $\sim 0.35$ – $0.55$  in the optical/UV, and  $\sim 0.65$  at high-energy  $\gamma$ -rays—consistent with expectations for high-synchrotron-peaked blazars. Segmenting the  $\gamma$ -ray light curve with Bayesian blocks, we defined 253 time-resolved epochs with adequate multi-band coverage and categorized them into quiescent states (QS), multiwavelength flares (MWF),  $\gamma$ -ray flares ( $\gamma$ F), X-ray flares (XF), and optical/UV flares (OUF). Each SED is modeled within a one-zone synchrotron self-Compton (SSC) framework that self-consistently evolves particle injection and cooling; a neural-network surrogate is used to accelerate parameter inference. Kolmogorov–Smirnov tests reveal state-dependent parameter variations relative to QS: (i) during MWF, the magnetic field  $B$ , electron luminosity  $L_e$ , maximum electron Lorentz factor  $\gamma_{\max}$ , and Doppler factor  $\delta$  differ significantly; (ii) during  $\gamma$ F, a harder electron index  $p$  is estimated; (iii) XF shows higher  $B$  and  $\gamma_{\max}$  with a more compact emitting region; and (IV) during OUF, changes in  $B$ ,  $L_e$ ,  $\gamma_{\max}$ ,  $\delta$ , and  $p$  are found while the emitting-zone size remains approximately constant. The jet power is electron-dominated (magnetic-to-electron power ratio  $\eta_B \simeq 0.09$ – $0.17$ ), with  $\eta_B$  rising during XF. These results suggest that variations in acceleration efficiency and magnetization drive band-dependent flaring in PKS 2155-304.

**Key words:** quasars: individual: PKS 2155-304; galaxies: jets; radiation mechanisms: non-thermal; gamma-rays: galaxies; X-rays: galaxies

## 1 INTRODUCTION

Blazars are a subclass of radio-loud active galactic nuclei in which a relativistic jet is viewed at a small angle to the line of sight of the observer (Urry & Padovani 1995). Because of the small viewing angle and relativistic motion of the jet, relativistic beaming amplifies the jet emission, producing some of the characteristic blazar features, including: extreme apparent luminosities, rapid broadband variability, high and variable polarization, and superluminal motion. One of the main defining feature of the blazar emission is the variability: the flux can increase by orders of magnitude on minute timescales (e.g., Ackermann et al. 2016; Shukla et al. 2018; Aleksić et al. 2014) or even seconds (e.g., Aharonian et al. 2007). Even if the emission from blazars is predominantly stochastic, a few sources have shown quasi-periodic oscillations in the  $\gamma$ -ray band (e.g., Ackermann et al. 2015; Peñil et al. 2020; Ren et al. 2023; Abdollahi et al. 2024), whose statistical significant detection remains an ongoing challenge.

The broadband emission of blazars spans from the radio to the high-energy (HE;  $> 100$  MeV) and very-high-energy (VHE;  $> 100$  GeV)  $\gamma$ -ray band, and exhibits a characteristic two-hump structure in the  $\nu F_\nu$  representation (for a review, see e.g. Padovani et al. 2017).

The first component peaks between the IR band and the X-ray band. It is generally interpreted as synchrotron radiation from relativistic electrons. The second, HE component (peaking above the X-ray band) can be produced from leptonic or hadronic processes. In leptonic scenarios, it can be produced via inverse Compton scattering—either of synchrotron photons (SSC; Ghisellini et al. 1985; Maraschi et al. 1992; Bloom & Marscher 1996) or of external photon fields such as photons from the accretion disk (Dermer et al. 1992; Dermer & Schlickeiser 1994), reflected from the broad-line region (Sikora et al. 1994), or from the dusty torus (Blažejowski et al. 2000). Instead, in hadronic interpretations, the HE component is attributed to proton-synchrotron emission (Mücke & Protheroe 2001) and/or cascades from photo-pion and photo-pair interactions (Mannheim 1993; Mannheim & Biermann 1989; Mücke & Protheroe 2001; Mücke et al. 2003; Böttcher et al. 2013; Petropoulou & Mastichiadis 2015; Gasparyan et al. 2022). The hadronic (specifically lepto-hadronic) models have become increasingly attractive following the detection of VHE neutrinos from the direction of blazars, including TXS 0506+056 (e.g., IceCube Collaboration et al. 2018a,b; Padovani et al. 2018) and PKS 0735+178 (e.g., Sahakyan et al. 2023)—as well as after statistical studies linking blazars and neutrino events (e.g., Plavin et al. 2020; Paiano et al. 2021). These detection

<sup>\*</sup> E-mail: narek.sahakyan@icranet.org

allowed for multimessenger studies of these sources which allowed to better constrain the processes taking place in their jets.

In general, blazars are commonly classified into two groups by the strength of their optical emission lines: BL Lacertae objects (BL Lacs), which show weak or absent lines, and flat-spectrum radio quasars (FSRQs), which display strong broad lines (Urry & Padovani 1995). Another classification of blazars is based on the frequency of the synchrotron peak  $\nu_p$ , dividing sources into low-synchrotron-peaked (LSP/LBL,  $\nu_p < 10^{14}$  Hz), intermediate-synchrotron-peaked (ISP/IBL,  $10^{14} < \nu_p < 10^{15}$ ), and high-synchrotron-peaked (HSP/HBL,  $\nu_p > 10^{15}$  Hz) blazars (Padovani & Giommi 1995; Abdo et al. 2010).

The origin of the broadband emission in blazars and the physical changes in jets that drive flaring activities are active research problems. Although the quantity and quality of the observed data is increasing and the theoretical models are becoming more sophisticated, time-resolved blazar SED modeling is still limited. To the exception of a few works, see e.g. Sahakyan (2021); Sahakyan & Giommi (2022); Sahakyan et al. (2022); Mohana A et al. (2025); Harutyunyan et al. (2025), most studies fit an average state, a single-epoch or at most a few snapshot SEDs. This is largely due to (*i*) the effort required to assemble strictly contemporaneous broadband data for a given source—often involving reprocessing and homogenization of heterogeneous archives—and (*ii*) the computational cost of time-dependent radiative models that track particle injection and cooling while exploring high-dimensional parameter space. When time-dependent models are coupled to rigorous inference (e.g., full posterior sampling rather than local optimization), fitting many SEDs becomes numerically intensive.

To address these issues, we recently developed two complementary tools: (*i*) the Markarian Multi-wavelength Data Center (MMDC; Sahakyan et al. 2024a), a novel data center that enables access and retrieval of multi-wavelength and multi-messenger blazar data, including both data from various catalogs and newly analyzed data in the optical/UV, X-ray, and  $\gamma$ -ray bands; and (*ii*) convolutional neural-network surrogate models trained on synthetic SEDs that include SSC (Bégué et al. 2024), EIC (Sahakyan et al. 2024b), and hadronic models (Sahakyan et al. 2025). This promising machine learning approach was also used by Tzavellas et al. (2024) in the context of blazars and by Boersma & van Leeuwen (2023) for gamma-ray bursts. These surrogates reproduce the radiative signatures of electrons and protons in the jet and can be coupled with Bayesian inference to fit SEDs efficiently without long computations. Together, these two tools streamline the construction of time-resolved datasets from blazar observations and enable scalable modeling of large number of SEDs, improving constraints on the physical processes in blazar jets.

To investigate the origin of blazar-jet emission and its time-dependent evolution, we initiated the Modeling of time-resolved Spectral Energy Distributions of blazars (MSED) project, which uses the two tools mentioned above. As a first case study, we analyzed blazar OJ 287, assembling and modeling 739 quasi-simultaneous SEDs within a one-zone SSC model (Harutyunyan et al. 2025). This enabled to track the temporal evolution of key model parameters and to identify distinct emission states characterized by specific parameter combinations (magnetic field  $B$ , electron index  $p$ , and Doppler boost  $\delta$ ). The second target we studied within the MSED project is the subject of this paper, namely PKS 2155-304, a HSP blazar at redshift  $z = 0.117$  (Bowyer et al. 1984). PKS 2155-304 is one of the brightest HBL objects and shows pronounced variability across different bands. For example, hour-scale variability has been observed in the X-ray band (e.g., Kataoka et al. 2000), and minute-scale variability has been observed at VHE  $\gamma$ -ray band (Aharonian et al. 2007). This

source has been frequently monitored in different bands, yielding a large, well-sampled dataset, which makes PKS 2155-304 an ideal target for time-resolved studies of the broadband emission during different activity states using (quasi-)simultaneous multi-band data.

In this paper, we investigate the physical processes at work in the jet of PKS 2155-304 by modeling its broadband emission across different emission states. We use optical/UV, X-ray, and  $\gamma$ -ray observations and construct a large set of SEDs from quasi-simultaneous measurements. Each SED is fitted with a one-zone SSC model, and we analyze the distributions of the physical parameters to quantify their evolution across states. This allowed us to quantify the changes in the jet properties responsible for the variation of the emission. The paper is organized as follows. Section 2 describes the data sets, their reductions, and the light-curve and spectra creation. Section 3 presents the time-resolved SED construction and its temporal evolution. Section 4 summarizes the theoretical model and inference setup. Section 5 reports statistical analysis of the parameters obtained from the modeling in different states. Section 6 provides the conclusions.

## 2 DATA ANALYSIS

In investigating the multiwavelength emission of PKS 2155-304, we used data from MMDC which is an open-access platform that provides time-resolved SEDs for blazars, combining archival catalog data with newly processed observations in the optical/UV, X-ray, and  $\gamma$ -ray bands (Sahakyan et al. 2024a). We note that the data can also be downloaded from the *firmamento* platform (Tripathi et al. 2024). The MMDC platform also enables SED modeling within leptonic models (SSC and EIC; Bégué et al. 2024; Sahakyan et al. 2024b)—as well as hadronic and lepto-hadronic models (Sahakyan et al. 2025). From MMDC, both SEDs and multi-band light curves are used to investigate the temporal evolution of the emission from PKS 2155-304. Below we present the analysis method applied to generate the data and summarize the main results; for more details on the analysis methods, we refer to Sahakyan et al. (2024a).

### 2.1 $\gamma$ -ray data

Since the launch of the *Fermi* Large Area Telescope (*Fermi*-LAT) in 2008, the  $\gamma$ -ray emission of PKS 2155-304 has been monitored continuously. *Fermi*-LAT is a pair-conversion  $\gamma$ -ray telescope sensitive to photons from 20 MeV to 300 GeV and, in survey mode, scans the entire sky approximately every three hours. A full description of the instrument is provided by Atwood et al. (2009).

The analysis follows the standard *Fermi*-LAT point-source procedures and is described in detail in Sahakyan et al. (2024a); the key steps are summarized here. We analyzed data from 2008 August 4 to 2023 July 4 (Mission Elapsed Time 239667417–710178221) using *Fermi*tools v2.0.8 with the P8R3\_SOURCE\_V3 instrument response functions. Events in the 100 MeV–300 GeV range were selected from a region of interest (ROI) of radius  $12^\circ$  centered on PKS 2155-304 position (RA =  $329.71^\circ$ , Dec =  $-30.22^\circ$ ). We used evclass=128 (SOURCE class) and evtype=3 (FRONT+BACK) events, and applied a zenith-angle cut of  $< 90^\circ$  to suppress Earth-limb contamination. The source model included all cataloged  $\gamma$ -ray emitters within  $17^\circ$  of the target selected from the 4FGL incremental catalog (DR3; Abdollahi et al. 2022). Parameters of sources within  $12^\circ$  were left free during the fit, while those outside this radius were fixed to their catalog values. The spectra of the sources were assumed to be identical to those used in the 4FGL-DR3 catalog. The

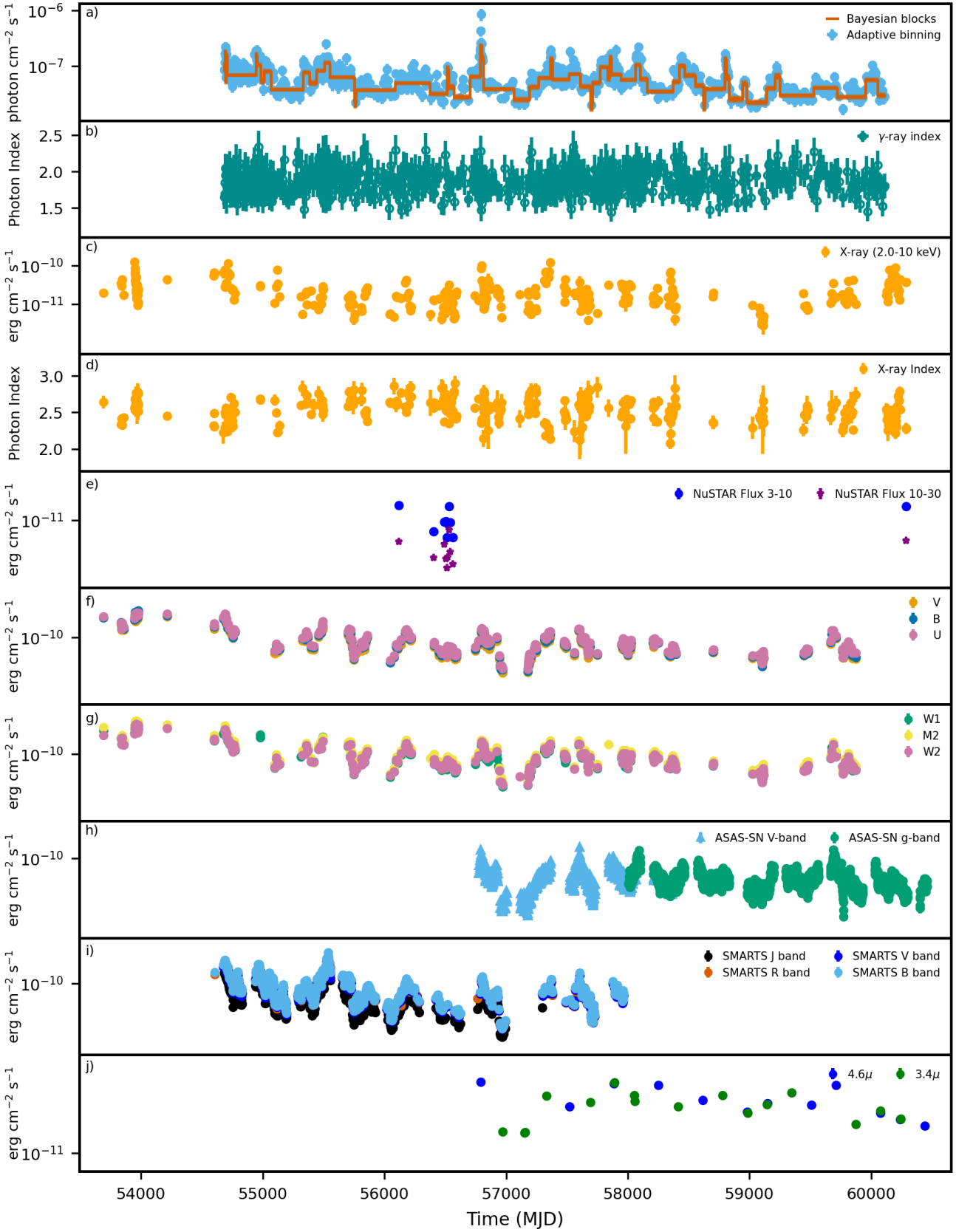


**Figure 1.** Multiwavelength light curves of PKS 2155-304. (a)  $\gamma$ -ray light curve (light-blue adaptive bins) with Bayesian-block segmentation (orange step curve) used to define time-resolved SED intervals. (b)  $\gamma$ -ray photon index. (c) *Swift*/XRT 2 – 10 keV flux. (d) Photon index in different XRT observations. (e) NuSTAR fluxes in 3 – 10 keV (blue diamonds) and 10 – 30 keV (magenta pentagons). (f) *Swift*/UVOT U, B, V fluxes. (g) *Swift*/UVOT W1, M2, W2 fluxes. (h) ASAS-SN g- and V-band fluxes. (i) Fluxes in J, V, R, B bands from SMARTS observations. (j) NEOWISE W1 ( $3.4\mu\text{m}$ ) and W2 ( $4.6\mu\text{m}$ ) fluxes (weighted means over  $\leq 10$  days windows).

Galactic diffuse emission (`gll_iem_v07`) and the isotropic component (`iso_P8R3_SOURCE_V3_v1`) were adopted with the latest recommended templates. We performed a binned maximum-likelihood analysis to optimize the spectral parameters.

Using the optimized model, we derived the  $\gamma$ -ray light curve of PKS 2155-304 with an adaptive-binning approach (Lott et al. 2012). Instead of regular fixed time step, in this method the time bin width is chosen such that the relative flux uncertainty above the optimal energy ( $E_{\text{opt}} = 276.9$  MeV for PKS 2155-304) reaches a value of 20%. Consequently, bins are shorter during bright states and longer during quiescence. For each interval then an unbinned likelihood analysis was applied assuming a simple power-law spectrum for PKS 2155-304 (appropriate for short intervals), applying the same event selections and background components as above. Adaptive binning has been widely used to identify and characterize flaring activity in blazars (e.g., Rani et al. 2013; Britto et al. 2016; Sahakyan & Gasparyan 2017; Zargaryan et al. 2017; Baghmanyan et al. 2017; Gasparyan et al. 2018; Sahakyan et al. 2018; Sahakyan 2021; Sahakyan et al. 2022; Sahakyan & Giommi 2022).

The  $\gamma$ -ray light curve of PKS 2155-304 is shown in Figure 1 (a); the corresponding photon index,  $\Gamma$ , is shown in Figure 1 (b). The light curve exhibits several episodes in which the  $\gamma$ -ray flux rises to  $\sim 3 \times$  the long-term mean of  $7.32 \sim 10^{-8}$  photon  $\text{cm}^{-2} \text{s}^{-1}$ , e.g., near MJD 54693.5, 55517.8, 56789.0–56794.0, and 58089.6. The most prominent  $\gamma$ -ray outburst occurred in May–June 2014: it began around MJD 56783 (2014-05-05), peaked at MJD 56794.7 (2014-05-17), and declined by MJD 56817 (2014-06-09), for a duration of  $\approx 34$  days. At the peak, the flux reached  $8.44 \sim 10^{-7}$  photon  $\text{cm}^{-2} \text{s}^{-1}$  ( $> 276.9$  MeV) with a very hard photon index of  $\Gamma \approx 1.47$ . During this flare the spectrum hardened as the flux increased and then softened toward  $\Gamma \sim 2.0$  during the decay. Similar episodes—flux enhancements accompanied by spectral hardening—are observed in other periods as well (see Figure 1 a and b), indicating that this behavior is common for PKS 2155-304 in the  $\gamma$ -ray band.

## 2.2 X-ray data

In the X-ray band, PKS 2155-304 has been regularly monitored by XRT on board the Neil Gehrels Swift Observatory (Gehrels et al. 2004, hereafter Swift) in the 0.3–10 keV band and with the Nuclear Spectroscopic Telescope Array (*NuSTAR*; Harrison et al. 2013) in the 3–79 keV band. Their joint coverage enables soft-to-hard X-ray investigation of PKS 2155-304 emission over more than two orders of magnitude in energy.

### 2.2.1 *Swift* XRT

*Swift*/XRT made 343 observations of PKS 2155-304 until July 4 2023. All blazar observations performed by *Swift* have been analyzed and processed, following the method detailed in Sahakyan et al. (2024a) and are made publicly available through the MMDC platform Sahakyan et al. (2024a). Here we summarize main steps relevant to reducing the observational data. The data have been processed with the `swift_xrtproc` pipeline (Giommi et al. 2021), which automatically downloads observation and calibration files, runs `xrtpipeline` to generate cleaned event files and exposure maps for each snapshot and the full observation, and performs standard analysis. Source and background spectra are extracted using a 20-pixel source aperture when the observation is not piled up and a source-free annulus for the background; pile-up is explicitly checked and, when present, spectra are re-extracted from an annulus with the inner radius set

by the measured count rate. Ancillary response files are built with `xrtmkarf` and appropriate response matrices from CALDB. Spectra (0.3–10 keV) are fitted in XSPEC (Arnaud 1996) with a power law model assuming a fixed Galactic absorption  $N_{\text{H}}$  (using `phabs` model); best-fit models are then converted to  $\nu F_{\nu}$  for SED construction. Further details on `swift_xrtproc` are provided in Giommi et al. (2021).

The variation of the X-ray flux (2–10 keV) and photon index ( $\Gamma_X$ ) in time are presented in Figure 1, panels c and d respectively. In the X-ray band, several flaring episodes are evident when the flux exceeds the long-term mean of  $\langle F_{2-10} \rangle \simeq 2.3 \times 10^{-11}$  erg  $\text{cm}^{-2} \text{s}^{-1}$ . The brightest flare occurred at MJD 53945 (2006-07-29), when the flux reached  $(1.25 \pm 0.02) \times 10^{-10}$  erg  $\text{cm}^{-2} \text{s}^{-1}$ —a factor of  $\sim 5.4$  above the mean—with  $\Gamma_X = 2.56 \pm 0.01$ . The second-highest flux was observed at MJD 57363 (2015-12-07),  $(1.21 \pm 0.15) \times 10^{-10}$  erg  $\text{cm}^{-2} \text{s}^{-1}$ , with a harder spectrum,  $\Gamma_X = 2.13 \pm 0.06$ . Overall,  $\Gamma_X$  spans  $\simeq 2.1$ – $2.9$ . The hardest spectrum,  $\Gamma_X = 2.07 \pm 0.07$  was observed at MJD 58347 (2018-08-17) with a flux of  $(6.5 \pm 0.9) \times 10^{-11}$  erg  $\text{cm}^{-2} \text{s}^{-1}$ , whereas the softest,  $\Gamma_X = 2.90 \pm 0.10$ , was measured at MJD 56578 (2013-10-13) at  $(4.7 \pm 0.9) \times 10^{-12}$  erg  $\text{cm}^{-2} \text{s}^{-1}$ . These show strong spectral and flux variability in the X-ray band, with episodes of both spectral hardening and softening.

### 2.2.2 *NuSTAR*

*NuSTAR* with its two focal plane modules, FPMA and FPMB (Harrison et al. 2013) observed PKS 2155-304 11 times; nine of these observations fall within the analysis window considered here. All data of blazars that were observed with *NuSTAR*, including PKS 2155-304, are available via MMDC. Here, we summarize the main points of the analysis. The data were processed with the automated *NuSTAR\_Spectra* pipeline (Middei et al. 2022), built on NuSTARDAS. The pipeline i) downloads the observations and calibration files; ii) generates a 3–20 keV image to derive the count rate to set extraction radii; iii) localizes the source with `XIMAGE`; and iv) runs `nuproducts` to create high-level science products. Source and background regions are chosen automatically with radii that scale with the measured count rate (typical the source radius is  $\approx 30$ – $70''$  while the background is from an annulus separated by  $\gtrsim 50''$ ). Then, the spectra are grouped to  $\geq 1$  count per bin and the data are fitted in XSPEC from 3 keV up to the energies when the background starts to dominate (often 20–79 keV) using Cash statistics (Cash 1979) and assuming a power law model and then computing the fluxes in the 3–10 and 10–30 keV bands. Finally, X-ray SED points are computed from 3 keV up to the energies where the net source signal exceeds the local background. For more details see Middei et al. (2022).

In Figure 1 panel (e), the variation of the fluxes in the 3–10 and 10–30 keV bands is shown displaying moderate variability, especially in the hard X-ray band. In the 3–10 keV band the flux changes from  $5.6 \times 10^{-12}$  to  $1.7 \times 10^{-11}$  erg  $\text{cm}^{-2} \text{s}^{-1}$  (mean  $\approx 10^{-11}$  erg  $\text{cm}^{-2} \text{s}^{-1}$ ) while in the 10–30 keV band, it varies between  $2.0 \times 10^{-12}$  and  $7.2 \times 10^{-12}$  erg  $\text{cm}^{-2} \text{s}^{-1}$  (mean  $3.7 \times 10^{-12}$  erg  $\text{cm}^{-2} \text{s}^{-1}$ ). This corresponds to variability amplitudes of  $\sim 3.0$  (3–10 keV) and  $\sim 3.6$  (10–30 keV). The brightest epochs occur at MJD 56116.7 and 56530.8, where the 3–10 keV flux reached  $(1.67 \pm 0.17) \times 10^{-11}$  and  $(1.61 \pm 0.16) \times 10^{-11}$  erg  $\text{cm}^{-2} \text{s}^{-1}$ , respectively. The *NuSTAR* photon index spans a relatively narrow range,  $\Gamma_X = 2.58$ – $3.03$  (mean  $\langle \Gamma_X \rangle \simeq 2.80$ ). The hardest spectrum,  $\Gamma = 2.58$ , was measured at MJD 56489.965 with 3–10 and 10–30 keV fluxes being  $9.4 \times 10^{-12}$  and  $4.4 \times 10^{-12}$  erg  $\text{cm}^{-2} \text{s}^{-1}$ , respectively. The softest spectrum,  $\Gamma \simeq 3.03$ , was observed at MJD 56506.939 with corresponding fluxes of  $9.7 \times 10^{-12}$  and  $2.7 \times 10^{-12}$  erg  $\text{cm}^{-2} \text{s}^{-1}$ . The soft indices

in this band indicate that the *NuSTAR* band observes the declining, high-energy tail of the synchrotron component which is characteristic for HSP blazars.

### 2.3 Optical/UV data

*Swift*/UVOT observed PKS 2155-304 in six filters in the optical (V: 500–600 nm; B: 380–500 nm; U: 300–400 nm) and ultraviolet (UVW1: 220–400 nm; UVM2: 200–280 nm; UVW2: 180–260 nm) bands providing information on the low energy component of the emission spectrum. UVOT data for all blazars observed by Swift (including PKS 2155-304) are accessible via MMDC. Here, we summarize only the main analysis steps. Data reduction was performed using an automated pipeline that follows standard UVOT analysis procedures, with photometry extracted from a 5'' aperture centered on the target and the background estimated from nearby source-free regions (from a 20'' region). Each image was inspected for contamination, and calibrated magnitudes were converted to fluxes using established zero-points and corrected for Galactic extinction based on  $E(B-V)$  values from the Infrared Science Archive. For further details, see Sahakyan et al. (2024a).

The optical and ultraviolet light curves are shown in Figure 1 (panels e and f). Variability is detected in all *Swift*/UVOT filters, with the source alternating between flaring and quiescent states. The highest flux of  $3.13 \times 10^{-10}$  erg cm $^{-2}$  s $^{-1}$ , was observed in M2 band on MJD 53960.85, exceeding the time-averaged flux in the same filter,  $1.18 \times 10^{-10}$  erg cm $^{-2}$  s $^{-1}$ , by a factor of 2.7. Among the remaining filters, the highest flux is  $2.78 \times 10^{-10}$  erg cm $^{-2}$  s $^{-1}$  in W2 filter on the same epoch, which is 2.6 times higher than the time-averaged flux in this band  $1.05 \times 10^{-10}$  erg cm $^{-2}$  s $^{-1}$ . Across the UVOT bands, the ratio of the highest and lowest fluxes ( $F_{\max}/F_{\min}$ ) are V = 8.15, B = 7.90, U = 7.04, W1 = 8.29, M2 = 8.27, and W2 = 7.99, indicating comparable but band-dependent variability.

In the optical band, we include additional data from the All-Sky Automated Survey for Supernovae (ASAS-SN; Kochanek et al. 2017) in the V and g filters. The corresponding light curve is shown in Figure 1 panel h. The ASAS-SN light curve exhibits variability consistent with *Swift*/UVOT observations. The mean flux over the monitoring period is  $5.8 \times 10^{-11}$  erg cm $^{-2}$  s $^{-1}$ . The brightest epoch occurred at MJD 57604.14, when the flux reached  $1.31 \times 10^{-10}$  erg cm $^{-2}$  s $^{-1}$ ; the faintest state was at MJD 59771.34 with the flux of  $2.37 \times 10^{-11}$  erg cm $^{-2}$  s $^{-1}$ , corresponding to ratio of  $\sim 5.5$  between the highest and lowest fluxes. These long-term optical measurements show pronounced variability of PKS 2155-304 emission in the optical band.

### 2.4 Archival and VHE $\gamma$ -ray data

In addition to the data described above, we retrieved multi-band observations of PKS 2155-304 from MMDC. Some of these datasets are from catalogs that lack reliable time measurements; therefore these data are used only to construct the time-averaged SED of PKS 2155-304. In contrast, time-resolved datasets—such as data from the Near-Earth Object Wide-field Infrared Survey Explorer (NEOWISE; Mainzer et al. 2011) and the Small and Moderate Aperture Research Telescope System (SMARTS; Bonning et al. 2012) allow to investigate the temporal evolution in the IR and optical bands. The SMARTS lightcurves in the J, R, V, and B filters are shown in Figure 1, panel i, demonstrating clear variability in all bands. SMARTS monitoring shows a major optical flare around MJD 55500: the activity started after MJD 55400 and lasted several weeks.

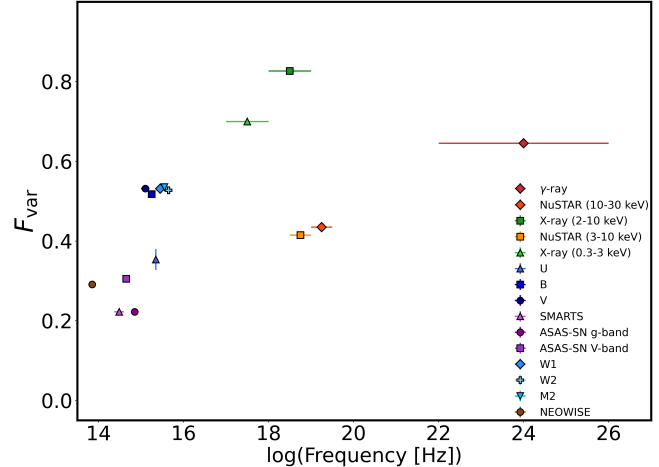


**Figure 2.** Fractional variability amplitude  $F_{\text{var}}$  as a function of frequency for PKS 2155-304. Symbols/colours denote bands as in the legend. Vertical error bars are  $1\sigma$  uncertainties on  $F_{\text{var}}$ ; horizontal bars indicate the width of each band.

This flare was detected quasi-simultaneously in all available bands (J, R, V and B). The brightest epoch occurred on MJD 55538.05, when the B-band flux reached  $2.34 \times 10^{-10}$  erg cm $^{-2}$  s $^{-1}$ , a factor of  $\sim 2.9$  above the long-term average flux from the SMARTS monitoring of PKS 2155-304 ( $\langle F \rangle \approx 8.2 \times 10^{-11}$  erg cm $^{-2}$  s $^{-1}$ ). Additional flares are present throughout the campaign, but this flare is the most prominent one. In the infrared band, NEOWISE observed PKS 2155-304 in different periods at 3.4 and 4.6  $\mu$ m. NEOWISE observations are organized in short campaigns spanning one to a few days approximately every six months. Therefore, in order to increase signal-to-noise ratio the observations with separation less than 10 days are grouped and combined using a weighted mean. The resulting light curve with the fluxes grouped around each observations is shown in Figure 1, panel j revealing moderate variability of the source in the IR band. The maximum weighted-mean flux at  $8.817 \times 10^{13}$  Hz (3.4  $\mu$ m) is  $(4.57 \pm 0.02) \times 10^{-11}$  erg cm $^{-2}$  s $^{-1}$  at MJD 56791.00, while at  $6.517 \times 10^{13}$  Hz (4.6  $\mu$ m) the peak is  $(3.81 \pm 0.01) \times 10^{-11}$  erg cm $^{-2}$  s $^{-1}$  at MJD 56791.03.

PKS 2155-304 is a well-known emitter in the VHE  $\gamma$ -ray band. To complete the broadband SED, we include published VHE observations of PKS 2155-304 by HESS from Aharonian et al. (2009) and Abdalla et al. (2020) and incorporate them into our dataset. When contemporaneous multi-band coverage exists, these points are included in the time-resolved SEDs. The VHE data provide crucial information at the highest energies, helping to constrain the second component in the SED of PKS 2155-304.

### 2.5 Fractional variability

In order to quantify the variability in different bands, we use the fractional variability  $F_{\text{var}}$  estimated following Schleicher et al. (2019). Figure 2 shows  $F_{\text{var}}$  as a function of frequency; horizontal bars indicate the frequency/bandwidth of each instrument/filter, and vertical bars show  $F_{\text{var}}$  and its uncertainty. The variability amplitude is strongly energy-dependent. In the infrared-optical bands (NEOWISE, SMARTS, ASAS-SN) the variability is low to moderate,  $F_{\text{var}} \sim 0.2$ –0.3. In the optical/UV bands (*Swift*/UVOT) the variability amplitude is higher,  $F_{\text{var}} \sim 0.35$ –0.55, showing more active states in the light curve. The variability is highest in soft/medium X-rays:

$F_{\text{var}} \sim 0.7$  in 0.3–3 keV and  $\sim 0.8$  in 2–10 keV bands. At harder X-rays (NuSTAR, 3–10 and 10–30 keV) the amplitude decreases to  $F_{\text{var}} \sim 0.42$ –0.44. In the HE  $\gamma$ -ray band the variability is moderate with  $F_{\text{var}} \approx 0.65$  (Figure 2).

This trend of fractional variability is overall expected for a blazar of type HSP. In the spectrum of this type of blazars, the emission in the infrared–optical bands are dominated by low-energy electrons with longer synchrotron cooling times, so the variability amplitude is shorter. Variability grows toward the soft/medium X-rays, which corresponds to the highest-energy tail of the synchrotron component; here acceleration and cooling timescales are shortest, so small changes in the injected electron population, magnetic field  $B$ , or Doppler factor  $\delta$  produce large flux changes. The moderate GeV-band variability is consistent with SSC-dominated inverse-Compton emission in HSPs: the IC component reflects the changes in the same electron population that powers the variability in the X-ray band, but the longer binning partially smooth out the rapid fluctuations.

### 3 TIME EVOLUTION OF THE MULTIWAVELENGTH SED

The datasets assembled above provide a comprehensive, multi-epoch view of the emission from PKS 2155-304 across the electromagnetic spectrum. This allows to build both a time-averaged SED and a series of time-resolved SEDs that track spectral evolution in different periods. For blazars, this distinction in time-resolved SEDs is essential: variability can shift the normalization and peak frequencies of both the synchrotron and inverse-Compton components. This combination of broad spectral coverage and temporal resolution in different periods is therefore critical to understand the origin of the emission and its changes in time.

In order to build the time resolved SED of PKS 2155-304 we adopt the SED/LC animation methodology used previously to study the source BL Lac (Sahakyan & Giommi 2022), 3C 454.3 (Sahakyan 2021), CTA 102 (Sahakyan et al. 2022), and OJ 287 (Harutyunyan et al. 2025). To build the SED/LC animation, we merge the multi-band light curves in Figure 1 with additional observational data from MMDC, then group the data that are simultaneous or quasi-simultaneous considering the  $\gamma$ -ray intervals as a base to build the time-resolved SEDs. Namely, the  $\gamma$ -ray light curve is segmented into smaller intervals with the Bayesian Blocks algorithm to define intervals of approximately constant flux (orange line in Figure 1, panel a). For each block, a dedicated spectral analysis of *Fermi*-LAT data is then performed with the method previously described in Section 2 to produce energy-resolved flux points (5 or 7 flux points, depending on the detection significance of the source in the considered interval). Data from all other bands that are within the Bayesian block window are then binned within the same block applying an adaptive time scan that subdivides the block into shorter windows to maximize simultaneity of the data while retaining sufficient data points. The resulting SEDs are plotted and changed sequentially—each aligned with its corresponding light-curve segment—to produce an SED/LC animation that tracks changes in the emission components. More implementation details on building SED/LC animation are provided in Sahakyan et al. (2024a).

The resulting SED/LC animation for PKS 2155-304 is available on Youtube at [SED/LC animation](#). It demonstrates the temporal evolution of the synchrotron and inverse-Compton components and enables to identify spectral component changes, peak-frequency shifts, flaring periods, etc. The broadband SED of PKS 2155-304 shows the traditional two-component structure, with the synchrotron peak at  $\nu_s \approx (1\text{--}5) \times 10^{16}$  Hz (UV–soft X-ray). Although the X-ray flux

varies substantially, the synchrotron peak frequency remains stable within uncertainties; variability is dominated by changes in flux with only mild curvature variations and no systematic shift in  $\nu_p$ . The variability is energy-band dependent and is consistent with the fractional-variability pattern: variability is small to moderate in the optical/UV, largest in the soft X-ray band, and moderate in the HE  $\gamma$ -ray band.

## 4 MODELING OF PKS 2155-304 SEDS

### 4.1 The SSC model

To model the broadband SEDs of PKS 2155-304, we adopt a one-zone leptonic synchrotron/SSC model (Ghisellini et al. 1985; Maraschi et al. 1992; Bloom & Marscher 1996). In this model, a spherical emission region of radius  $R$  moves relativistically along the jet with bulk Lorentz factor  $\Gamma$  and is viewed at a small angle  $\theta \sim 1/\Gamma$  with respect to the jet axis. The region contains a homogeneous magnetic field of strength  $B$  and a non-thermal population of relativistic electrons. The low-energy component of the SED, extending from radio to X-ray frequencies, is explained by synchrotron radiation from these electrons as they spiral in the jet magnetic field. The same population upscatters the synchrotron photons to HEs via the inverse Compton process, producing the HE component. In the current study, the model is computed using a novel neural-network-based method presented in Bégué et al. (2024). In this approach, the computationally expensive radiative calculations, including electrons cooling, are replaced by a CNN surrogate model, trained on a large set of synthetic SEDs generated with SOPRANO (Gasparyan et al. 2022) over a wide range of model parameters. SOPRANO self-consistently solves the coupled kinetic equations for electrons and photons—including particle injection and radiative cooling—and computes the corresponding SEDs. Once trained, the CNN accurately reproduces the radiative output of particles inside the jet while reducing the evaluation time by orders of magnitude, enabling fitting and parameter inference.

In this paper, the injection spectrum of the electron energy distribution is modeled as a power law with an exponential cut-off,

$$\dot{Q} = \begin{cases} Q_{e,0}\gamma^{-p} \exp\left(-\frac{\gamma}{\gamma_{\max}}\right) & \gamma > \gamma_{\min} \\ 0 & \text{otherwise} \end{cases} \quad (1)$$

where  $Q_{e,0}$  is the normalization such that the electron luminosity is  $L_e = \pi R^2 \delta^2 m_e c^3 \int_1^\infty \gamma Q_e d\gamma$ ,  $p$  is the electron power-law index,  $\gamma_{\min}$  is the minimum electron Lorentz factor at injection (electrons may cool to smaller Lorentz factors), and  $\gamma_{\max}$  is the maximum electron Lorentz factor. In addition, both electrons and photons are assumed to leave the emitting region in the characteristic dynamical time  $t = R/\Gamma$ . To conclude, the model has seven free parameters:  $p$ ,  $\gamma_{\min}$ ,  $\gamma_{\max}$ ,  $B$ ,  $R$ ,  $\delta$ , and the electron luminosity  $L_e$ , although in practice we do not fit for  $\gamma_{\min}$ , see below.

### 4.2 Fit method and classification

In the SED/light-curve animation discussed in Section 3, a total of 327 SEDs are available. However, not all of these can be reliably modeled due to insufficient observational coverage. Among them, only 253 SEDs have adequate multiwavelength coverage enough for the modeling: specifically, we require the availability of X-ray data together with measurements in the low-energy band, as the  $\gamma$ -ray data is available by default. These SEDs were therefore selected for

State	$B$ [10 <sup>-2</sup> G]	$L_e$ [10 <sup>44</sup> erg s <sup>-1</sup> ]	$\gamma_{\max}$ [10 <sup>5</sup> ]	$R$ [10 <sup>17</sup> cm]	$\delta$	$p$	$L_B$ [10 <sup>43</sup> erg s <sup>-1</sup> ]
QS	1.62 ± 0.02	9.14 ± 0.84	2.09 ± 0.01	3.31 ± 0.37	24.6 ± 6.1	2.30 ± 0.21	6.55 ± 3.19
MWF	4.78 ± 0.19	5.36 ± 1.69	4.87 ± 0.30	1.88 ± 0.11	24.8 ± 5.2	2.20 ± 0.13	18.5 ± 6.6
$\gamma$ F	1.71 ± 0.17	13.7 ± 8.5	1.83 ± 0.00	4.64 ± 0.47	18.2 ± 4.9	2.06 ± 0.09	7.78 ± 1.91
XF	1.64 ± 0.21	6.48 ± 6.14	9.81 ± 0.12	5.34 ± 0.72	18.8 ± 5.4	2.21 ± 0.14	10.1 ± 2.4
OUF	1.28 ± 0.14	11.1 ± 8.07	2.33 ± 0.01	5.63 ± 0.63	20.8 ± 5.4	2.17 ± 0.14	8.42 ± 2.43
Unclassified	1.56 ± 1.35	9.42 ± 6.56	1.51 ± 0.62	4.53 ± 3.91	23.0 ± 5.4	2.25 ± 0.14	9.98 ± 2.70

**Table 1.** Model parameters from one-zone SSC fits to the SEDs of PKS 2155-304 in the different states shown in Figure 3. These are provided as examples, but each of the 253 SEDs have been fitted and their parameters recovered.

modeling. The fits were performed using MultiNest, a nested sampling algorithm (Feroz et al. 2009). We adopted 1500 active points and a tolerance of 0.4, which ensures both efficient exploration of the parameter space and robust convergence of the posterior distributions. For the modeling, we fixed the minimum Lorentz factor of the electron distribution to  $\gamma_{\min} = 100$ . This choice is motivated by two considerations. First, the low-energy emission (below  $\sim 10^{10}$  Hz) is often produced in more extended regions of the jet, which are not well constrained by the compact one-zone model applied here. Second, observational data at low frequencies are not available in most of the SEDs selected here. Setting  $\gamma_{\min} = 100$  avoids introducing unconstrained degrees of freedom while remaining consistent with typical values adopted in blazar modeling. Finally, we note that extragalactic background light absorption at high energy is included by multiplying the emission model described in Section 4.1 by the model developed in Domínguez et al. (2011).

In order to have a quantitative discussion on the emission states of PKS 2155-304, the selected SEDs were grouped in different categories based on the activity states. Namely, the dataset was divided into three frequency ranges: optical/UV ( $3 \times 10^{14} - 10^{16}$  Hz), X-rays ( $10^{16} - 10^{21}$  Hz), and  $\gamma$ -rays ( $10^{21} - 10^{28}$  Hz). For each range, we computed the average flux and its standard deviation which serve as a baseline level. Then, the state of the source was classified in the following way. A multiwavelength flare (MWF) was identified when the flux in all three bands exceeded the archival average, whereas a quiescent state (QS) was defined when the flux in all bands is on average or remained below the average. If only the  $\gamma$ -ray flux was above the average while the UV/optical and X-ray bands were below, the episode was classified as a  $\gamma$ -ray flare ( $\gamma$ F). Similarly, an X-ray flare (XF) corresponded to a case where the X-ray flux was above the average while the other bands remained lower, and a UV/optical flare (OUF) was defined when only the optical/UV flux exceeded the average. A total of 117 SEDs were classified as QS, 18 as MWF, 7 as  $\gamma$ F, 20 as XF, and 31 as OUF. The remaining 61 SEDs display mixed characteristics in the mentioned bands and are left unclassified. This separation makes it possible to separate true multiwavelength flares from band-limited flares and quiescent states, thereby providing a clearer characterization of the variability pattern of PKS 2155-304 across the electromagnetic spectrum.

#### 4.3 Example of fit results for each category

Before studying in detail the statistical properties of each SED category, we provide for each one independently an example demonstrating the fitting performances and results.

An example of the SED corresponding to the QS is shown in the upper-left panel of Figure 3 and the corresponding parameters are given in Table 1. The red solid line represents the model obtained with the best-fit parameters, while the gray lines indicate the associated

uncertainties. In this state, the emission can be explained with (i) an electron power-law index  $p = 2.3$ , (2) a maximum Lorentz factor of the electron distribution  $\gamma_{\max} = 2.1 \times 10^5$ , (3) a magnetic field strength  $B = 1.6 \times 10^{-2}$  G, (4) an emitting region radius  $R = 3.3 \times 10^{17}$  cm, and (5) a Doppler factor  $\delta = 24.6$ . The total kinetic power carried by electrons is  $L_e = 9.1 \times 10^{44}$  erg s<sup>-1</sup>, while the power in the magnetic field, computed as  $L_B = \pi c R^2 \Gamma^2 U_B$ , is  $6.5 \times 10^{43}$  erg s<sup>-1</sup>.

The SED corresponding to the MWF is presented in the upper-right panel of Figure 3 with corresponding parameters in Table 1. In this case, the emission is produced from a region with a magnetic field of  $B = 4.8 \times 10^{-2}$  G and an electron kinetic power of  $L_e = 5.4 \times 10^{44}$  erg s<sup>-1</sup>. The maximum Lorentz factor of the electron distribution is  $\gamma_{\max} = 4.9 \times 10^5$ , indicating the presence of highly energetic particles in the emitting region. As we demonstrate below, these high energy electrons are characteristics of the MWF activity. The size of the emitting region is  $R = 1.9 \times 10^{17}$  cm, and the Doppler factor is  $\delta = 24.8$  demonstrating a significant relativistic boosting during this MWF. The electron energy distribution is characterized by a power-law index  $p = 2.20$ .

The SEDs corresponding to  $\gamma$ F, XF, and OUF states are shown in the middle and lower-left panels of Figure 3. In all cases, the broadband emission is well modeled with the SSC model used in this study, with the best-fit parameters for these examples summarized in Table 1. In the  $\gamma$ F state, the fit yields a magnetic field of  $B = 1.71 \times 10^{-2}$  G, an electron luminosity of  $L_e = 1.37 \times 10^{45}$  erg s<sup>-1</sup>, and a maximum Lorentz factor of  $\gamma_{\max} = 1.8 \times 10^5$ . The emitting region size is  $R \simeq 4.6 \times 10^{17}$  cm, and the Doppler factor is moderately low compared to other states ( $\delta \simeq 18.2$ ). The electron slope is harder than in the QS ( $p = 2.06$ ), consistent with harder particle injection during the  $\gamma$ -ray activity. In the XF state, the electron energy distribution reaches significantly higher cutoff energies, with  $\gamma_{\max} \simeq 9.8 \times 10^5$ , almost an order of magnitude larger than in the  $\gamma$ F and OUF states. This shift is accompanied by a relatively weak magnetic field ( $B = 1.64 \times 10^{-2}$  G) and large emission region ( $R \simeq 5.3 \times 10^{17}$  cm). The Doppler factor remains moderate ( $\delta \simeq 18.8$ ), while the electron luminosity is comparatively lower ( $L_e \simeq 6.5 \times 10^{44}$  erg s<sup>-1</sup>). These values indicate that the electrons are effectively accelerated to higher energies which drives the strong changes in the X-ray component. On the contrary, the OUF state is characterized by a higher magnetic field ( $B = 2.04 \times 10^{-2}$  G) and a more compact emission region ( $R \simeq 3.5 \times 10^{17}$  cm). The maximum Lorentz factor is the lowest among the flaring states ( $\gamma_{\max} \simeq 1.4 \times 10^5$ ), suggesting that the flare is dominated by the emission from low energy electrons rather than re-acceleration or injection of fresh energetic electrons. The Doppler factor remains high ( $\delta \simeq 23.9$ ), also in this case.

An example of modeling of the SED which was unclassified is shown in the lower-right panel of Figure 3, and the corresponding parameters are listed in Table 1. In this epoch, the optical/UV and

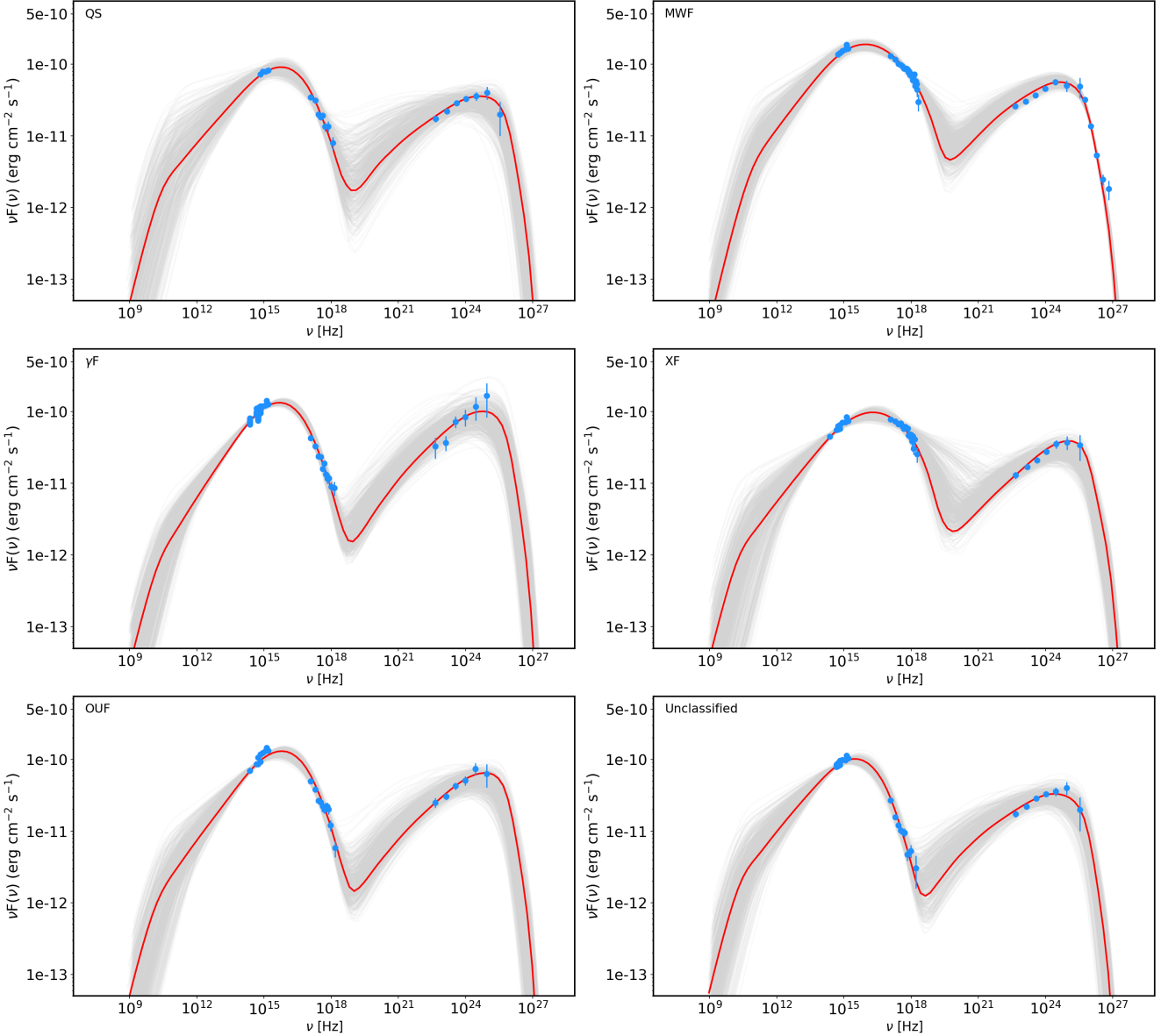


**Figure 3.** For each SED class, example of a multiwavelength SEDs of PKS 2155-304 modeled within the one-zone SSC framework. The blue points are the data, the red curve corresponds to the best-fit model (e.g., when the likelihood is maximum) and the gray spectra corresponds to the model uncertainty. Extragalactic background light absorption is included in the modeling using the model of Dominguez et al. (2011).

$\gamma$ -ray fluxes are consistent with their long-term averages, whereas the X-ray flux is comparatively low. In this case a one-zone SSC model reproduces the broadband SED well with parameters that are not substantially different than those obtained in the other cases.

As seen from these examples, while the SSC model provides a satisfactory description of the data in all cases, the key differences in the parameters during different states — namely, the high  $\gamma_{\max}$  in the XF state, the flatter electron spectrum in the  $\gamma$ F state, and the stronger magnetic field in the OUF state - show that distinct physical processes dominate in each activity state. These examples suggest that the spectral variability in PKS 2155-304 is not driven by a single mechanism, but rather by changes in the emitting particle or in the emission region. It is the purpose of Section 5 to demonstrate the statistical differences across the different emission episodes and isolate parameter changes responsible for changes in the spectrum

of PKS 2155-304, to enable a physical description of the different emission periods of PKS 2155-304.

#### 4.4 The previous modelings of PKS 2155-304

In contrast to earlier studies, where the modeling of PKS 2155-304 was performed for only a limited number of broadband SEDs, the analysis presented here considers modeling of a substantially larger number of SEDs. The results obtained in this study across different states are typical of those usually found for blazars and consistent with previous studies of PKS 2155-304. For example, Madejski et al. (2016) modeled the source during a low-flux state using contemporaneous multiwavelength data. Their results indicated that the emission can be explained with an electron energy distribution with an index  $p = 2.2$ , a break Lorentz factor  $\gamma_{\text{br}} \sim 2.6 \times 10^4$ , and a magnetic field strength of  $B \sim 0.5$  G, with a characteristic emitting region

radius of  $R \sim 1.3 \times 10^{16}$  cm. Most of these parameters (except  $B$ ) are within the range that we estimated for the QS, see Section 5. Another modeling of PKS 2155-304 was presented in Aleksić et al. (2012) based on the 2006 MAGIC campaign; the SED was modeled by adopting (and not fitting) the parameters  $\delta = 50$ ,  $B \simeq 0.085$  G, and  $R \simeq 9 \times 10^{15}$  cm. However, in their SED the contemporaneous HE  $\gamma$ -ray data were absent limiting the constraints provided by the inverse Compton component. The main difference between the results obtained here and these previous studies of PKS 2155-304 is that we performed modeling without assuming any specific initial spectral shape, instead exploring the global minima of the posterior distributions for each SED across many time periods.

## 5 STATISTICAL ANALYSIS OF THE DIFFERENT STATES

Multiwavelength modeling plays a central role in advancing our understanding of blazar emission, especially when different states can be compared. This approach allows to compare and contrast key model parameters, which in turn provides a direct link between the observed variability patterns and the underlying physical conditions in the jet. In this way, observational properties, e.g., the flux changes or spectral variability in different bands, can be connected with physical parameters characteristics of the emission region, such as the spectral slopes of the emitting particles, the magnetic field, the maximum energy of the electrons, etc. These can then be transformed into constraints on particle acceleration, energy dissipation, and radiation processes.

The modeling of the selected 253 time-resolved SEDs together with the time evolution of the posterior distributions of the model parameters is presented as an animation at [YouTube](#) synchronized with the corresponding light-curve intervals, connecting the evolution of both the multi-wavelength emission state and the SED modeling. The images from the animations are available on [GitHub](#). The temporal evolution of the parameters is shown in Figure 4, where different emission states are represented by distinct colors and symbols. Such a representation allows to evaluate changes in parameter space that are responsible for flaring activities when comparing with the light curve from Figure 1, either across the full multiwavelength band or within specific energy ranges, thereby offering clues about the physical origin of these events.

### 5.1 Statistical properties of the inferred model parameters

From modeling the 117 SEDs in the QS state we found that, the best-fit model parameters exhibit relatively narrow distributions. The electron power-law index is centered around a mean of  $p \simeq 2.24$  (median 2.22), varying between 1.90 and 2.68. The electrons maximum Lorentz factor spans nearly an order of magnitude, from  $\gamma_{\max} \simeq 7.2 \times 10^4$  to  $6.5 \times 10^5$ , with an average value of  $2.3 \times 10^5$ . The magnetic field strength is typically weak, ranging from  $B \simeq 2.3 \times 10^{-3}$  to  $1.8 \times 10^{-1}$  G, with a mean of  $2.6 \times 10^{-2}$  G. The size of the emitting region is large, with radii between  $R \simeq 4.7 \times 10^{16}$  and  $6.3 \times 10^{17}$  cm (mean  $3.8 \times 10^{17}$  cm). The Doppler factor varies moderately, with values from  $\delta \simeq 15.1$  to 42.7 (mean  $\sim 21.9$ ). The electron kinetic power is of the order of  $L_e \sim 10^{45}$  erg s $^{-1}$ , ranging from  $2.4 \times 10^{44}$  to  $8.3 \times 10^{45}$  erg s $^{-1}$ , with a mean value of  $1.0 \times 10^{45}$  erg s $^{-1}$ .

The modeling of the 18 SEDs identified as MWF shows that the magnetic field strength varies within  $B \simeq 1.5 \times 10^{-2}$  -  $7.0 \times 10^{-2}$  G, with an average value of  $2.9 \times 10^{-2}$  G. The electron luminosity varies in the range between  $4.8 \times 10^{44}$  erg s $^{-1}$  and  $2.4 \times 10^{45}$  erg s $^{-1}$  with a mean of  $1.1 \times 10^{45}$  erg s $^{-1}$ . The maximum Lorentz factor

of the electron distribution is between  $1.6 \times 10^5$  and  $5.8 \times 10^5$ , with a mean value of  $3.4 \times 10^5$ , which shows the presence of electrons accelerated to GeV energies during flares. The emission region is found to be relatively extended,  $R = 0.8 \times 10^{17}$ – $5.4 \times 10^{17}$  cm, with a mean radius of  $3.4 \times 10^{17}$  cm. The Doppler factors cluster around  $\delta \sim 24$ , ranging from 18.7 to 30.9, while the power-law index of electron energy distribution changes between  $p = 2.0$  and 2.6 with a mean of 2.23.

In the  $\gamma$ F state, the modeling shows that the emission regions are moderately extended,  $R \sim 0.9$ – $6.3 \times 10^{17}$  cm, with relatively weak magnetic fields,  $B \sim 1.3 \times 10^{-2}$ – $8.9 \times 10^{-2}$  G. The maximum energy of the electron distribution  $\gamma_{\max}$  is in the range between  $1.0 \times 10^5$  and  $2.5 \times 10^5$ , while the electron luminosity are in the range of  $L_e \sim (0.4$  –  $1.4) \times 10^{45}$  erg s $^{-1}$  with a mean of  $L_e = 8.4 \times 10^{44}$  erg s $^{-1}$ . In these periods, the power-law index of the electrons is stepper than in other ones, with  $p = 2.02$ – $2.18$ , indicating that more energy is present in the highest energy electrons, while the Doppler boost is in the range  $\delta \sim 17$  – 21.

In contrast, the modeling shows that XF have systematically higher electron maximum energies and magnetic field:  $\gamma_{\max}$  varies in the range of  $7.1 \times 10^4$  and  $1.8 \times 10^6$  with 70% of the estimated  $\gamma_{\max}$  being above  $2 \times 10^5$ . The magnetic field is stronger on average, varying between  $B \sim 1.6 \times 10^{-2}$  –  $0.3$  G, while the emission regions are somewhat more compact,  $R \sim 1.4 \times 10^{16}$ – $5.3 \times 10^{17}$  cm. The modeling of these flares also results in a high Doppler factor,  $\delta \sim 18.5$  – 32.2, consistent with enhanced beaming during strong X-ray activity, and the electron luminosity is in the range between  $9.0 \times 10^{43}$  erg s $^{-1}$  to  $L_e = 1.5 \times 10^{45}$  erg s $^{-1}$  with a mean of  $L_e = 6.06 \times 10^{44}$  erg s $^{-1}$ .

The modeling of SEDs in the OUF states shows yet another behavior: the magnetic field is moderate,  $B = 9.0 \times 10^{-3}$  –  $0.18$  G, with a mean of  $3.7 \times 10^{-2}$  G, but the emission regions are systematically larger,  $R = 1.4 \times 10^{16}$  –  $6.2 \times 10^{17}$  cm, with 89% of the cases having an emission region size exceeding  $10^{17}$  cm. The maximum Lorentz factor of the electrons is comparatively low,  $\gamma_{\max}$  is in the range between  $3.1 \times 10^4$  and  $2.6 \times 10^5$  which is similar to the values estimated in the  $\gamma$ F state but well below those estimated for XF. The Doppler boost is relatively strong varying in the interval  $\delta = 19.4$  – 43.5, and the electron luminosity is comparable to the values estimated in  $\gamma$ F, with  $L_e = 0.4$  –  $4.4 \times 10^{45}$  erg s $^{-1}$ .

To clearly display the differences between the different emission states, we show on Figure 5, the distributions of the parameters for different states separately. This comparison shows several general trends. (i) In most cases, the mean of the electron power-law index remains relatively stable around  $p \sim 2.1$  – 2.2, with only a modest hardening during XF and  $\gamma$ F. In contrast, (ii) the mean of the magnetic field shows a strong dependence on the spectral state: it is weakest in the QS and OUF ( $B \lesssim 0.03$  G), moderate during MWF and  $\gamma$ F, and highest in XF ( $B \gtrsim 0.08$  G), representing a variation of a factor of nearly 3 on average between the different states. The mean of the Doppler factor clusters around  $\delta \sim 20$  – 25 in most cases. (iii) The mean of the electron maximum Lorentz factor allows to distinguish the states very clearly: it is the highest in the MWF and XF ( $\gamma_{\max} \gtrsim 3 \times 10^5$ ), comparatively lower in OUF state ( $\gamma_{\max} = 1.5 \times 10^5$ ), and moderate in  $\gamma$ F ( $\gamma_{\max} = 1.7 \times 10^5$ ). (iv) The distribution of  $R$  shows relatively extended emission regions across all states, clustering around a few  $\times 10^{17}$  cm. While the median values do not differ drastically, XF exhibits the widest spread, with  $R$  reaching both the lowest and highest extremes among the states. In contrast, QS, MWF, OUF, and  $\gamma$ F tend to show more confined distributions with median values around  $3$  –  $4 \times 10^{17}$  cm. (v) The distribution of  $L_e$  is comparatively stable across all states, with mean values around  $10^{44.5}$  –  $10^{45}$  erg s $^{-1}$ . The QS exhibits a slightly

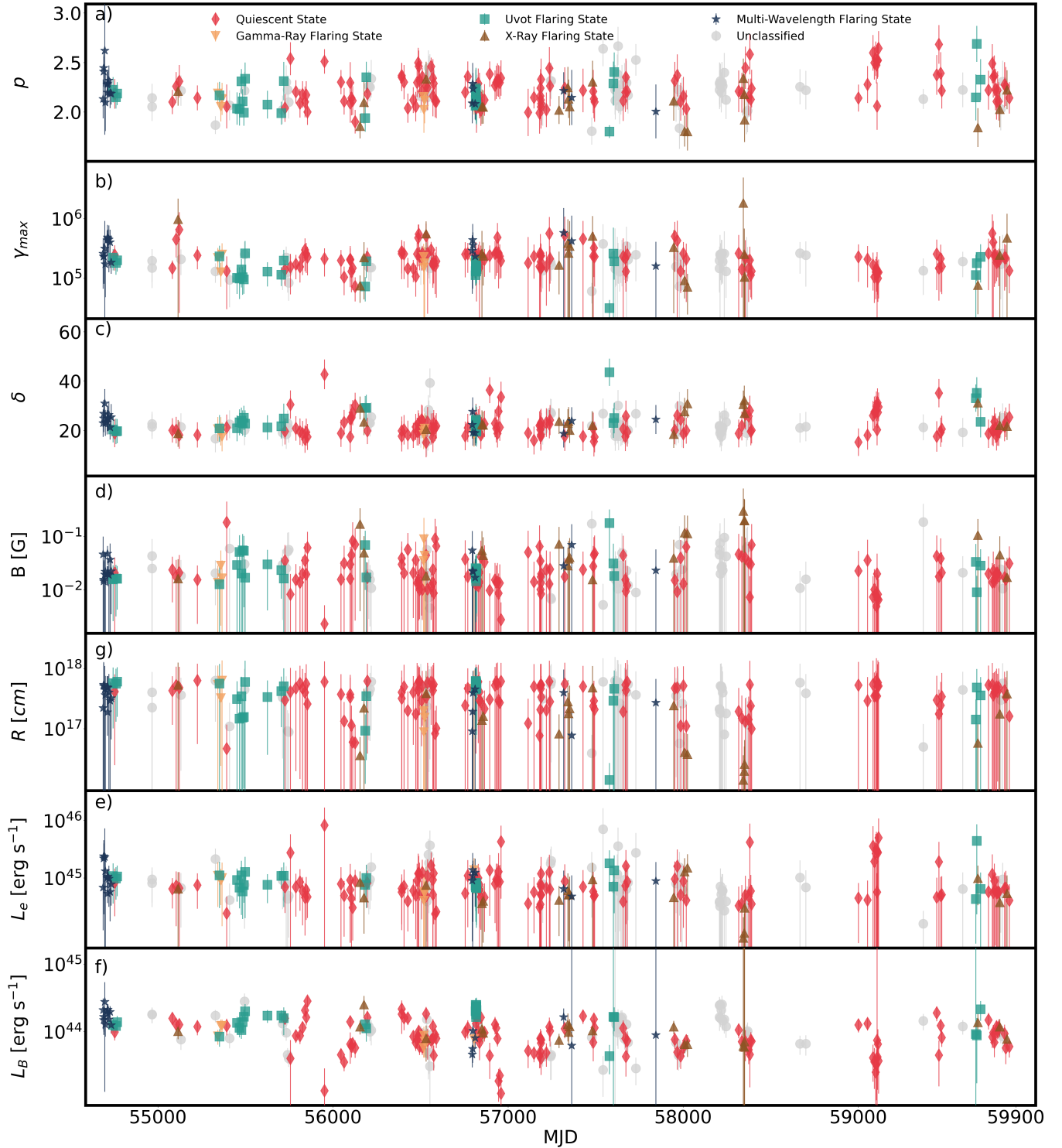


**Figure 4.** Time evolution of the one-zone SSC parameters for PKS 2155-304, derived from fitting the SEDs in different states. Panels show (a) the electron power-law index  $p$ , (b) the maximum electron Lorentz factor  $\gamma_{\max}$ , (c) the Doppler factor  $\delta$ , (d) the magnetic field  $B$  [G], (e) the emitting-region radius  $R$  [cm], (f) the electron kinetic power  $L_e$  [ $\text{erg s}^{-1}$ ], and (g) the (derived) magnetic power  $L_B$  [ $\text{erg s}^{-1}$ ] versus MJD. Colored symbols denote activity states as indicated in the legend.

**Table 2.** Results of the KS test, indicating if the parameter variation between any state and the QS are significant. The parameters are in this order:magnetic field ( $B$ ), electron luminosity ( $L_e$ ), maximum energy ( $\gamma_{\max}$ ), emission region size ( $R$ ), Doppler factor ( $\delta$ ), spectral index ( $p$ ).

State	$B$		$L_e$		$\gamma_{\max}$		$R$		$\delta$		$p$	
	KS	$p$	KS	$p$	KS	$p$	KS	$p$	KS	$p$	KS	$p$
MWF	0.338	0.045	0.359	0.027	0.474	$1.0 \times 10^{-3}$	0.252	0.236	0.410	0.007	0.137	0.899
$\gamma$ F	0.267	0.354	0.293	0.254	0.327	0.155	0.265	0.364	0.239	0.489	0.506	0.004
XF	0.545	$3.0 \times 10^{-5}$	0.301	0.072	0.338	0.030	0.519	$8.8 \times 10^{-5}$	0.390	0.008	0.405	0.005
OUF	0.316	0.007	0.381	$4.8 \times 10^{-4}$	0.418	$8.9 \times 10^{-5}$	0.143	0.581	0.290	0.016	0.283	0.021

broader spread, extending toward higher luminosities, while the flaring states (MWF, XF, and  $\gamma$ F) appear more clustered and show no systematic enhancement in  $L_e$ .

In order to investigate differences in the parameter distributions between the QS and other activity states, we performed Kolmogorov-Smirnov (KS) tests on the parameters. The results are summarized in Table 2, for each parameter providing the KS statistics and corresponding  $p$ -values (probability). We consider  $p$ -values below 0.05 (roughly corresponding to  $2\sigma$ ) as indicating statistically significant differences from the Quiet State distribution. For the MFW state, significant differences appear in  $B$  ( $p = 0.045$ ),  $L_e$  ( $p = 0.027$ ),  $\gamma_{\max}$  ( $p = 0.001$ ), and  $\delta$  ( $p = 0.007$ ), suggesting that these parameters change during flares compared to QS. In contrast,  $R$  and  $p$  show no notable differences ( $p > 0.2$ ), meaning that the emission region size and electron spectrum remain similar to the QS. In the  $\gamma$ F state, most parameters do not differ significantly from the QS, with  $p$ -values above 0.15 for  $B$ ,  $L_e$ ,  $\gamma_{\max}$ ,  $R$ , and  $\delta$ . However, the spectral index  $p$  shows a clear hardening ( $p = 0.004$ ), pointing to changes in the electron energy distribution during  $\gamma$ -ray flares. The largest number of parameter changes are observed during the XF state with significant  $p$ -values for  $B$  ( $p < 0.001$ ),  $\gamma_{\max}$  ( $p = 0.030$ ),  $R$  ( $p < 0.001$ ),  $\delta$  ( $p = 0.008$ ), and  $p$  ( $p = 0.005$ ). Only  $L_e$  does not show significant changes ( $p = 0.072$ ), indicating that X-ray flares involve broad changes in the magnetic fields, emission geometry, beaming, as well as in the particle distribution, but electron luminosity is comparable to quiescence. For the OUF state, we find significant differences in all parameters except  $R$  ( $p = 0.581$ ). For the other parameters, the significance is given by  $B$  ( $p = 0.007$ ),  $L_e$  ( $p < 0.001$ ),  $\gamma_{\max}$  ( $p < 0.001$ ),  $\delta$  ( $p = 0.016$ ), and  $p$  ( $p = 0.021$ ). This suggests that flares in the optical/UV bands are the results of changes in magnetic fields, electron properties, and beaming, while the emission region size does not deviate much from the QS.

Overall, these KS test results show state-dependent variations in the physical parameters. The XF and OUF states show the strongest departures from QS, particularly for  $\gamma_{\max}$  and  $\delta$ . This could be due to enhanced particle acceleration and relativistic effects during flaring activities. The limited changes in the  $\gamma$ F state, except  $p$ , suggest that  $\gamma$ -ray flares might be due to different mechanisms, which affects the electron spectrum but not the other parameters.

## 5.2 Physical interpretation

The modeling across different periods reveals state-dependent changes in several parameters that inform the emission scenario. The electron power-law index varies during the  $\gamma$ F, XF, and OUF states but remains within  $p \approx 1.8$ – $2.7$ , i.e., within the range expected from shock-acceleration theory. Indices near  $\approx 2.0$  are characteristic of diffusive shock acceleration (Bell 1978; Blandford & Ostriker 1978; Blandford & Eichler 1987), while softer or harder spectra can arise in relativistic shocks (Kirk & Schneider 1987; Ellison et al. 1990; Bed-

narz & Ostrowski 1998; Ellison & Double 2004). Alternatively, such indexes can also be produced in magnetic-reconnection events (Giannios 2013; Lyutikov & Uzdensky 2003; Lyubarsky 2005; Giannios et al. 2009; Petropoulou et al. 2016).

During the  $\gamma$ F state the electron spectrum hardens, with  $p \approx 2.0$ – $2.3$ . This is consistent with temporarily more efficient acceleration (e.g., higher shock compression, changes in turbulence anisotropy, or a larger effective mean-free-path ratio near the shock). The modeling does not show a significant increase in  $\gamma_{\max}$  during  $\gamma$ F, consistent with the relatively unchanged X-ray flux during these periods. As the other parameters do not change significantly, the  $\gamma$ -ray flares are more naturally attributed to changes in the injection/acceleration spectrum rather than to extended acceleration that raises the maximum energy or to changes in the emission-region size, parameters which remain statistically constant compared to the QS.

In the XF state, the inferred increase in  $B$  aligns with the observed X-ray variability pattern: the X-ray flux rises while the photon index remains soft (see Figure 1, panels c and d). Because the X-rays probe the high-energy tail of the synchrotron component, a higher  $B$  shifts the synchrotron peak upward and produces a higher peak flux without requiring a hardening of the electron slope.

During OUF, the fitted parameters are broadly consistent with those in other states, but the injected slope spans a wider range,  $p \approx 1.8$ – $2.7$ . This spread is expected because the optical/UV band samples the rising part of the synchrotron component, where the observed slope is sensitive to the locations of the synchrotron peak and the cooling break. Small changes in  $B$  or  $\delta$  can move these features across the band, and modest curvature can be absorbed by the fit as changes in  $p$ . Moreover, if the  $\gamma$ -ray spectrum remains nearly unchanged while the optical/UV flux and shape vary, joint fits can accommodate a broader range of  $p$ .

In MWF states, the pattern indicates enhanced magnetic fields, increased power injected into electrons, and changes in bulk motion that affect beaming, while  $R$  and  $p$  show no systematic change within uncertainties. Thus, the geometry of the emitting region and the overall electron-slope shape appear roughly stable; flares are mainly driven by plasma variations that modify the magnetic field and the acceleration conditions.

The inferred parameters for the emission region size  $R$  in all the periods suggest that the radiation originates from an extended region in the jet. This implies that the characteristic variability time, computed as  $t_{\text{var}} = (1+z)R/(\delta c)$ , is of several days across all states: for the average state, with average  $R \approx 3.85 \times 10^{17}$  cm and average  $\delta \approx 21.9$ ,  $t_{\text{var}} \approx 7.6$  days; in the XF state ( $R \approx 1.86 \times 10^{17}$  cm,  $\delta \approx 24.5$ ),  $t_{\text{var}} \approx 3.3$  days; or in the UVOF state ( $R \approx 3.89 \times 10^{17}$  cm,  $\delta \approx 24.2$ ),  $t_{\text{var}} \approx 7.0$  days, etc. This indicates that the flaring activity occurs over relatively large scales, without the rapid flux changes.

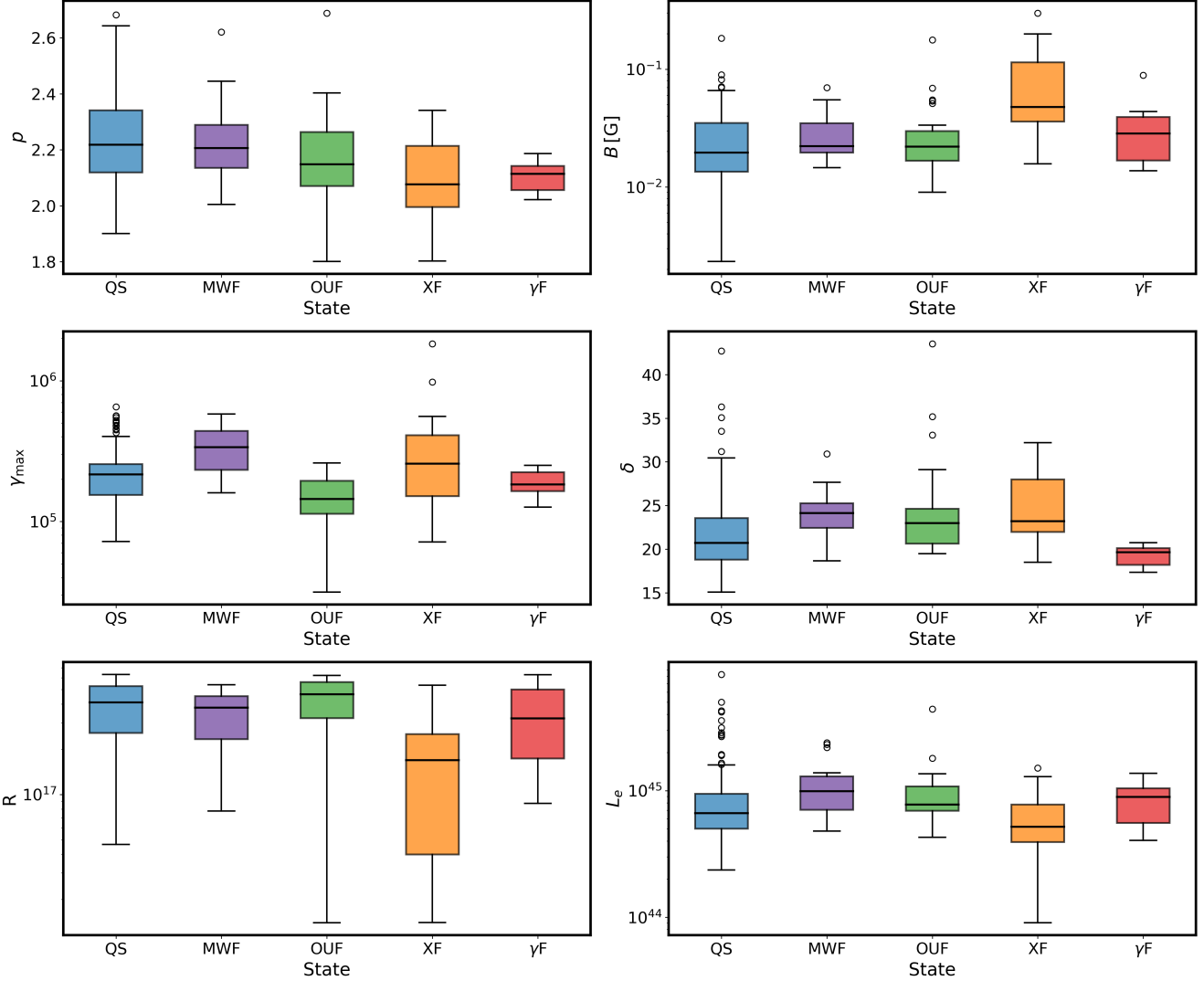


**Figure 5.** The distributions of all model parameters  $p$ ,  $B$  [G],  $\gamma_{\max}$ ,  $\delta$ ,  $R$  [cm] and  $L_e$  [ $\text{erg} \cdot \text{s}^{-1}$ ] for different states represented as box plots. The central line marks the median, box edges correspond to the 25th and 75th percentiles, whiskers extend to  $1.5 \times$  the interquartile range, and outliers are plotted as circles. Qualitatively, the X-ray–flaring state tends to show larger  $B$ , while  $\gamma$ -ray–flaring states favor slightly harder  $p$  and lower  $\delta$  and  $\gamma_{\max}$  relative to other states.

### 5.3 Jet energetics

We examine the jet energetics, and in particular the luminosity carried by electrons and magnetic field in different activity states. We use the power ratio  $\eta_B \equiv L_B/L_e$  to measure the magnetization of the jet. Because  $L_{e,B} \propto \pi R^2 T^2 c u'_{e,B}$ , the common geometric/beaming factor cancels in the ratio, so  $\eta_B$  primarily shows the internal energy partition rather than beaming characteristics. Using the averaged mean values, the power ratio for each independent state is:  $\eta_B \approx 0.1$  (electron-dominated by a factor  $\sim 11$ ) in QS,  $\eta_B \approx 0.13$  ( $\sim 7.9$ ) in MWF state,  $\eta_B \approx 0.12$  ( $\sim 8.6$ ) in  $\gamma$ F state,  $\eta_B \approx 0.17$  ( $\sim 5.9$ ) in XF state and  $\eta_B \approx 0.16$  ( $\sim 6.2$ ) in OUF. Thus, the jet is particle-dominated in all states ( $\eta_B \approx 0.09 - 0.17$ ). The jet is closest to the equipartition during XF: a higher  $B$  results in a larger  $u'_B \propto B^2$  and hence  $L_B$ , while  $L_e$  does not change significantly. On the contrary in  $\gamma$ F,  $\eta_B$  is lower than for XF which supports the scenario that  $\gamma$ -ray brightening is mainly driven by particle injection properties, producing a steeper index, rather than by an increased magnetization, or variation of other parameters.

## 6 CONCLUSIONS

We presented a comprehensive time-resolved multiwavelength study of the HSP blazar PKS 2155-304, using extensive archival and processed data from the MMDC platform. Using observational data in the  $\gamma$ -ray, X-ray, optical, ultraviolet and IR bands, we have investigated the source variability in these bands and examined the origin of the emission through modeling the time-resolved SEDs in the different emission states.

The analysis showed energy-dependent variability, with the fractional variability amplitude peaking in the soft to medium X-ray regime ( $0.7 - 0.8$ ) - while remaining moderate in the optical/UV ( $0.35 - 0.55$ ) and HE  $\gamma$ -ray bands ( $\approx 0.65$ ). This pattern aligns with expectations for HSP blazars, where synchrotron emission from HE electrons drives rapid variations in X-rays, contrasted by more stable contributions at lower energies.

Through Bayesian block segmentation of the  $\gamma$ -ray light curve, we generated 253 well-sampled time-resolved SEDs with quasi-simultaneous data, classifying them into distinct activity states: QS, MWF,  $\gamma$ F, XF, and OUF. The modeling of these SEDs within a

one-zone SSC scenario shows state-dependent parameter changes that are statistically significant compared to QS. KS tests show that MWF episodes differ in  $B$ ,  $L_e$ ,  $\gamma_{\max}$ , and  $\delta$ , while  $R$  and  $p$  are consistent with QS.  $\gamma$ -ray flares are distinguished by a harder electron index  $p$  (with other parameters not significantly changed), indicating that the  $\gamma$ -ray brightening is due to changes in the particle injection/acceleration process leading to steeper electron spectra. XF states show the broader changes in the parameters: higher  $B$  and  $\gamma_{\max}$ , smaller  $R$ , and higher  $\delta$ —consistent with enhanced acceleration and magnetization driving the strong X-ray flares. OUF states differ in  $B$ ,  $L_e$ ,  $\gamma_{\max}$ ,  $\delta$ , and  $p$ , but not in  $R$ , suggesting that optical/UV activity is produced by moderate changes in magnetization, boost, and the HE cutoff without geometric changes. During all the flaring periods, the jet energetics is dominated by the electrons luminosity rather than the magnetic luminosity, with power ratios  $\eta_B \approx 0.09 - 0.17$ , which is approaching to equipartition during X-ray-dominant activity.

The results obtained here show the complex interplay of magnetic fields, particle acceleration, and relativistic beaming in producing flares in blazar emission, highlighting the value of long-term, multi-epoch modeling for these events for a better understanding of the origin of the flares.

## ACKNOWLEDGEMENTS

The research was supported by the Higher Education and Science Committee of MESCS RA (Research project No 23LCG-1C004). MK acknowledge the support by the Higher Education and Science Committee of the Republic of Armenia, in the frames of the research project No 24AA-1C039.

We acknowledge the use of services from the Markarian Multi-wavelength Data Center ([www.mmdc.am](http://www.mmdc.am)).

## DATA AVAILABILITY

All the data used in this paper is available from MMDC ([www.mmdc.am](http://www.mmdc.am)). The data is also available upon reasonable request to the corresponding author.

## REFERENCES

- Abdalla H., et al., 2020, *A&A*, **639**, A42  
 Abdo A. A., et al., 2010, *ApJ*, **716**, 30  
 Abdollahi S., et al., 2022, *ApJS*, **260**, 53  
 Abdollahi S., et al., 2024, *ApJ*, **976**, 203  
 Ackermann M., et al., 2015, *ApJ*, **813**, L41  
 Ackermann M., et al., 2016, *ApJ*, **824**, L20  
 Aharonian F., et al., 2007, *ApJ*, **664**, L71  
 Aharonian F., et al., 2009, *ApJ*, **696**, L150  
 Aleksić J., et al., 2012, *A&A*, **544**, A75  
 Aleksić J., et al., 2014, *Science*, **346**, 1080  
 Arnaud K. A., 1996, in Jacoby G. H., Barnes J., eds, Astronomical Society of the Pacific Conference Series Vol. 101, Astronomical Data Analysis Software and Systems V. p. 17  
 Atwood W. B., et al., 2009, *ApJ*, **697**, 1071  
 Baghmanyan V., Gasparyan S., Sahakyan N., 2017, *ApJ*, **848**, 111  
 Bednarz J., Ostrowski M., 1998, *Phys. Rev. Lett.*, **80**, 3911  
 Bégué D., Sahakyan N., Dereli-Bégué H., Giommi P., Gasparyan S., Khachaturyan M., Casotto A., Pe'er A., 2024, *ApJ*, **963**, 71  
 Bell A. R., 1978, *MNRAS*, **182**, 147  
 Blandford R., Eichler D., 1987, *Phys. Rep.*, **154**, 1  
 Blandford R. D., Ostriker J. P., 1978, *ApJ*, **221**, L29  
 Błażejowski M., Sikora M., Moderski R., Madejski G. M., 2000, *ApJ*, **545**, 107  
 Bloom S. D., Marscher A. P., 1996, *ApJ*, **461**, 657  
 Boersma O. M., van Leeuwen J., 2023, *Publ. Astron. Soc. Australia*, **40**, e030  
 Bonning E., et al., 2012, *ApJ*, **756**, 13  
 Böttcher M., Reimer A., Sweeney K., Prakash A., 2013, *ApJ*, **768**, 54  
 Bowyer S., Brodie J., Clarke J. T., Henry J. P., 1984, *ApJ*, **278**, L103  
 Britto R. J., Bottacini E., Lott B., Razzaque S., Buson S., 2016, *ApJ*, **830**, 162  
 Cash W., 1979, *ApJ*, **228**, 939  
 Dermer C. D., Schlickeiser R., 1994, *ApJS*, **90**, 945  
 Dermer C. D., Schlickeiser R., Mastichiadis A., 1992, *A&A*, **256**, L27  
 Domínguez A., et al., 2011, *MNRAS*, **410**, 2556  
 Ellison D. C., Double G. P., 2004, *Astroparticle Physics*, **22**, 323  
 Ellison D. C., Jones F. C., Reynolds S. P., 1990, *ApJ*, **360**, 702  
 Feroz F., Hobson M. P., Bridges M., 2009, *MNRAS*, **398**, 1601  
 Gasparyan S., Sahakyan N., Baghmanyan V., Zargaryan D., 2018, *ApJ*, **863**, 114  
 Gasparyan S., Bégué D., Sahakyan N., 2022, *MNRAS*, **509**, 2102  
 Gehrels N., et al., 2004, *ApJ*, **611**, 1005  
 Ghisellini G., Maraschi L., Treves A., 1985, *A&A*, **146**, 204  
 Giannios D., 2013, *MNRAS*, **431**, 355  
 Giannios D., Uzdensky D. A., Begelman M. C., 2009, *MNRAS*, **395**, L29  
 Giommi P., et al., 2021, *MNRAS*, **507**, 5690  
 Harrison F. A., et al., 2013, *ApJ*, **770**, 103  
 Harutyunyan G., Sahakyan N., Bégué D., 2025, *MNRAS*, **540**, 582  
 IceCube Collaboration et al., 2018a, *Science*, **361**, 147  
 IceCube Collaboration et al., 2018b, *Science*, **361**, eaat1378  
 Kataoka J., Takahashi T., Makino F., Inoue S., Madejski G. M., Tashiro M., Urry C. M., Kubo H., 2000, *ApJ*, **528**, 243  
 Kirk J. G., Schneider P., 1987, *ApJ*, **315**, 425  
 Kochanek C. S., et al., 2017, *PASP*, **129**, 104502  
 Lott B., Escande L., Larsson S., Ballet J., 2012, *A&A*, **544**, A6  
 Lyubarsky Y. E., 2005, *MNRAS*, **358**, 113  
 Lyutikov M., Uzdensky D., 2003, *ApJ*, **589**, 893  
 Madejski G. M., et al., 2016, *ApJ*, **831**, 142  
 Mainzer A., et al., 2011, *ApJ*, **731**, 53  
 Mannheim K., 1993, *A&A*, **269**, 67  
 Mannheim K., Biermann P. L., 1989, *A&A*, **221**, 211  
 Maraschi L., Ghisellini G., Celotti A., 1992, *ApJ*, **397**, L5  
 Middei R., Giommi P., Perri M., Turriziani S., Sahakyan N., Chang Y. L., Leto C., Verrecchia F., 2022, *MNRAS*, **514**, 3179  
 Mohana A. K., et al., 2025, *The Astrophysical Journal*, **989**, 125  
 Mücke A., Protheroe R. J., 2001, *Astroparticle Physics*, **15**, 121  
 Mücke A., Protheroe R. J., Engel R., Rachen J. P., Stanev T., 2003, *Astroparticle Physics*, **18**, 593  
 Padovani P., Giommi P., 1995, *ApJ*, **444**, 567  
 Padovani P., et al., 2017, *A&ARv*, **25**, 2  
 Padovani P., Giommi P., Resconi E., Glauch T., Arsioli B., Sahakyan N., Huber M., 2018, *MNRAS*, **480**, 192  
 Paiano S., Falomo R., Treves A., Padovani P., Giommi P., Scarpa R., 2021, *MNRAS*, **504**, 3338  
 Peñil P., et al., 2020, *ApJ*, **896**, 134  
 Petropoulou M., Mastichiadis A., 2015, *MNRAS*, **447**, 36  
 Petropoulou M., Giannios D., Sironi L., 2016, *MNRAS*, **462**, 3325  
 Plavin A., Kovalev Y. Y., Kovalev Y. A., Troitsky S., 2020, *ApJ*, **894**, 101  
 Rani B., Lott B., Krichbaum T. P., Fuhrmann L., Zensus J. A., 2013, *A&A*, **557**, A71  
 Ren H. X., Cerruti M., Sahakyan N., 2023, *A&A*, **672**, A86  
 Sahakyan N., 2021, *MNRAS*, **504**, 5074  
 Sahakyan N., Gasparyan S., 2017, *MNRAS*, **470**, 2861  
 Sahakyan N., Giommi P., 2022, *MNRAS*, **513**, 4645  
 Sahakyan N., Baghmanyan V., Zargaryan D., 2018, *A&A*, **614**, A6  
 Sahakyan N., Israyelyan D., Harutyunyan G., Gasparyan S., Vardanyan V., Khachaturyan M., 2022, *MNRAS*, **517**, 2757  
 Sahakyan N., Giommi P., Padovani P., Petropoulou M., Bégué D., Boccardi B., Gasparyan S., 2023, *MNRAS*, **519**, 1396  
 Sahakyan N., et al., 2024a, *AJ*, **168**, 289

- Sahakyan N., et al., 2024b, [ApJ, 971, 70](#)
- Sahakyan N., Bégué D., Casotto A., Dereli-Bégué H., Vardanyan V., Khachaturyan M., Giommi P., Pe'er A., 2025, [The Astrophysical Journal](#), 990, 222
- Schleicher B., et al., 2019, [Galaxies](#), 7, 62
- Shukla A., et al., 2018, [ApJ](#), 854, L26
- Sikora M., Begelman M. C., Rees M. J., 1994, [ApJ](#), 421, 153
- Tripathi D., et al., 2024, [AJ](#), 167, 116
- Tzavellas A., Vasilopoulos G., Petropoulou M., Mastichiadis A., Stathopoulos S. I., 2024, [A&A](#), 683, A185
- Urry C. M., Padovani P., 1995, [PASP](#), 107, 803
- Zargaryan D., Gasparyan S., Baghmanyan V., Sahakyan N., 2017, [A&A](#), 608, A37

This paper has been typeset from a  $\text{\TeX}/\text{\LaTeX}$  file prepared by the author.